crystals

MDPI

Article

Design, Preparation and Synergistic Optimization of Mechanical Properties and Thermal Neutron Shielding Performance of Mg-Dy-Sm-Zr Alloys

Huabing Lu [1], Chengzhi Duan [1], Enci Niu [1], Xiyu Xu [2], Jia She [1,3], Jun Tan [1,3], Wei Zhang [2,*] and Jianjun Mao [2,*]

[1] Department of Material Science, College of Materials Science and Engineering, Chongqing University, Chongqing 400044, China; 202309131207@stu.cqu.edu.cn (H.L.)
[2] The First Research Institute of China, Nuclear Power Research and Design Institute, Chengdu 610005, China
[3] National Engineering Research Center for Magnesium Alloys, Chongqing University, Chongqing 400044, China
* Correspondence: zw812@npic.ac.cn (W.Z.); mao0707@npic.ac.cn (J.M.)

Abstract

Addressing the challenge of synergistically optimizing shielding performance and mechanical properties in nuclear radiation shielding materials, this study designed and prepared as-cast Mg-12Dy-xSm-0.4Zr (x = 1, 2, 3) alloys by incorporating rare earth elements Dy and Sm, which possess high thermal neutron absorption cross-sections. The co-addition of Sm and Dy significantly refined the grains and promoted the precipitation of bone-like Mg_5(Sm,Dy) and $Mg_{41}Sm_5$ phases along grain boundaries. The alloys exhibited favorable mechanical properties, with ultimate tensile strength (UTS) reaching up to 194.6 MPa and elongation (EL) up to 10.9%. However, higher Sm content led to an increased amount of secondary phases at grain boundaries, resulting in stress concentration and a subsequent decline in both yield strength and elongation. Moreover, the combined addition of Dy and Sm markedly enhanced the thermal neutron shielding performance. Experimental results agreed well with Geant4 simulations, showing that both the neutron shielding rate and linear attenuation coefficient improved with increasing Sm content, demonstrating the positive role of Dy and Sm in neutron absorption. The developed alloy achieves simultaneous improvement in mechanical properties and neutron shielding capacity, providing valuable insights for the development of lightweight "function–structure integrated" radiation shielding materials for applications such as nuclear medicine and aerospace.

Keywords: neutron shielding material; Mg alloy; Geant4; integration of structure and function

check for updates

Academic Editors: Changling Zhuang and Patrice Berthod

Received: 17 September 2025
Revised: 6 October 2025
Accepted: 10 October 2025
Published: 15 October 2025

Citation: Lu, H.; Duan, C.; Niu, E.; Xu, X.; She, J.; Tan, J.; Zhang, W.; Mao, J. Design, Preparation and Synergistic Optimization of Mechanical Properties and Thermal Neutron Shielding Performance of Mg-Dy-Sm-Zr Alloys. *Crystals* **2025**, *15*, 894. https://doi.org/10.3390/cryst15100894

Copyright: © 2025 by the authors. Licensee MDPI, Basel, Switzerland. This article is an open access article distributed under the terms and conditions of the Creative Commons Attribution (CC BY) license (https://creativecommons.org/licenses/by/4.0/).

1. Introduction

Nuclear energy, as a clean and efficient energy source, plays an irreplaceable role in addressing the global energy crisis, reducing greenhouse gas emissions, and promoting sustainable development [1]. The radiation generated by nuclear reactions includes α and β particles, X-rays, γ-rays, neutrons, and protons. Among these, neutrons exhibit extremely high penetration power and pose the greatest hazards to both humans and equipment [2]. With the widespread application of nuclear technology in fields such as energy, medicine, and aerospace, neutron radiation shielding has become a critical aspect of ensuring operational safety of equipment and health of personnel.

Currently, neutron shielding materials mainly fall into four categories: metal-based, polymer-based, glass-based, and concrete materials [3–6]. However, each type has significant limitations. In metal-based materials, although borated stainless steel offers good

high-temperature stability and corrosion resistance [7], excessive boron leads to the precipitation of brittle phases such as $(Fe,Cr)_2B$, significantly reducing plasticity and toughness [3]. B_4C/Al composites exhibit high specific strength but face challenges, such as particle agglomeration and interfacial reactions (e.g., formation of brittle phases like Al_3BC) [8,9]. Polymer-based materials, such as boron-containing polyethylene, possess excellent shielding and processing properties but suffer from poor heat resistance. Prolonged irradiation typically reduces the molecular weight of polymers, lowers the softening temperature, and to some extent increases material solubility [10]. Glass-based materials, while offering transparency, experience degraded mechanical properties due to the addition of heavy metal oxides, making them unsuitable for structural applications [11]. Concrete, being cost-effective, safe, and of high strength, serves as an economical choice for radiation shielding in nuclear reactors [12]. However, its heavy weight and large volume make it difficult to meet the demands of mobile equipment or lightweight applications. These drawbacks have prompted researchers to explore novel multifunctional materials. Therefore, developing new materials that integrate efficient neutron shielding performance, excellent mechanical properties, and structural functionality has become a core requirement for the sustainable development of nuclear technology.

As the lightest metallic structural material currently available, magnesium alloys combine high specific strength, excellent damping capacity, and good manufacturability, demonstrating significant potential for applications in aerospace and nuclear industries [13]. However, pure magnesium exhibits extremely low neutron absorption cross-section [14]. Rare earth (RE) elements have emerged as key modifiers for functionalizing magnesium alloys due to their unique neutron shielding properties and strengthening effects. Existing studies [15–18] have confirmed the application potential of RE elements in radiation protection—for instance, shielding materials containing gadolinium (Gd) have been relatively well-studied [19], while RE elements have also shown considerable advantages in structural magnesium alloys [20,21]. Nevertheless, research on RE-containing magnesium alloys for shielding remains limited.

Current studies by Le et al. have demonstrated that increasing Gd content in Mg-Gd alloys significantly improves the thermal neutron attenuation coefficient, while maintaining structural stability under irradiation conditions of 200 °C and 10 dpa Au^+ ions [22]. Samarium (Sm) possesses an exceptionally high thermal neutron absorption cross-section of 40,080 B(barns), and its transmutation products also exhibit high neutron absorption capacity [23]. The eutectic solubility of Sm in Mg is 5.8 wt%. Therefore, the addition of Sm not only enhances the neutron absorption capacity but also improves the mechanical properties through grain refinement and the formation of precipitates [24]. Dysprosium (Dy), with a neutron absorption cross-section of 2650 B(barns), produces extended decay chains under neutron irradiation, enabling Dy-containing materials to maintain effective neutron absorption performance throughout long-term reactor operation [25]. Dy exhibits a maximum solid solubility of 25.8 wt% in magnesium at 561 °C, exceeding that of Gd and Y. When temperature decreases to 200 °C, its solubility dramatically reduces to 10.2%, indicating significant potential for both solid solution and age hardening. Appropriate Dy addition can notably refine magnesium alloy grains [26]. Zirconium (Zr), as an important alloying element, is widely used in magnesium alloys to enhance their strength, ductility, creep resistance and corrosion resistance [27,28].

Based on these advantages, a novel neutron shielding material—Mg-Dy-Sm-Zr alloy—has been designed. This alloy is expected to overcome the conventional trade-off between shielding capacity and mechanical properties, achieving integrated functionality in both neutron absorption and structural load-bearing. Given the differences in solid solubility and neutron absorption cross-section between Sm and Dy, this study

systematically varies Sm content while investigating the correlation among RE element composition, microstructure, thermal neutron shielding performance, and mechanical properties, with particular focus on Sm-Dy synergistic effects. This work offers guidance for designing new neutron shielding materials and broadens the potential for using magnesium alloys in lightweight radiation shielding applications, which is of great scientific and engineering relevance.

2. Materials and Methods

2.1. Materials

The as-cast alloys with a nominal composition of Mg-12Dy-xSm-0.4Zr (in mass fraction, wt.%), where x = 1, 2, and 3 wt%, were designed and are hereafter referred to as DS1, DS2, and DS3, respectively. The experimental materials were prepared from pure Mg ingot (99.95%) and Mg–30Dy, Mg–30Sm, and Mg–20Zr master alloys. Melting was conducted in an electric resistance furnace using a heat-resistant low-carbon steel crucible under a protective atmosphere consisting of 99% CO_2 and 1% SF_6. Subsequently, after an isothermal holding time of 10 min, the molten mixture was poured into a steel mold preheated to 400 °C. In order to compare the effects of adding rare earth elements, the smelting experiment also used pure magnesium ingots to undergo the same smelting process for pouring to obtain the cast pure magnesium, and then conducted subsequent performance tests as well. The actual contents of rare earth elements in the alloys were verified by inductively coupled plasma (ICP) analysis. The results, summarized in Table 1, confirm that the measured compositions are consistent with the designed values. Using Archimedes' principle of displacement, the densities of the three alloys were measured to be 1.88, 1.90, and 1.92 g/cm^3.

Table 1. The ICP test results of rare earth elements.

Sample	Dy (wt%)	Sm (wt%)
Mg-12Dy-1Sm-0.4Zr	12.38 ± 0.05	1.03 ± 0.05
Mg-12Dy-2Sm-0.4Zr	12.65 ± 0.05	2.11 ± 0.05
Mg-12Dy-3Sm-0.4Zr	12.54 ± 0.05	3.06 ± 0.05

2.2. Microstructural Characterization

The sample was polished step by step from 400# to 4000# using gold phase sandpaper. Then, the polished surface was mechanically polished with gold phase polishing agent. Finally, the sample was etched with 6% nitric acid alcohol for 40 s to obtain the OM and SEM observation samples. The microstructure of the alloy was observed using an optical microscope (OM). The secondary electron image of the sample was observed using a scanning electron microscope (SEM) with test parameters of 15 kV and 13 μA. The distribution and size of the constituent phases were further studied. The sample processing flow for XRD was the same as that for the gold phase samples. The anode target material used was copper target Cu-Kα (λ = 0.1542 nm), with a scanning angle range of 10 to 90 degrees, a scanning speed of 2°/min, a working voltage of 40 kV, and a filament current of 40 mA. The collected data was analyzed using the MDI Jade 9. The sample was processed into a 0.5 mm thin sheet using wire cutting. The sample was prepared using the dry–wet dual-purpose sandpaper grinding method, and then reduced to 100 μm. A φ3 circular sample was made using a puncher, and further reduced using an ion thinning instrument with a thinning voltage of 5.5 kV to obtain the TEM observation sample. TEM and STEM analyses were conducted at an accelerating voltage of 200 kV.

2.3. Mechanical Properties

Tensile tests were conducted at room temperature using a CMT6305-300KN universal testing machine (SUST, Xi'an, China) at a constant crosshead speed of 1 mm/min to determine the yield strength (YS), ultimate tensile strength (UTS), and elongation (EL) of the alloys. The tensile test specimen geometry is illustrated in Figure 1. To ensure accuracy and reproducibility, tests were performed in triplicate. Micro-Vickers hardness measurements were carried out on the alloy surfaces using an HVS-1000Z hardness tester (Cossim, Shanghai, China) under a load of 200 gf with a dwell time of 10 s. Twenty indentations were performed for each sample, and the average hardness value was calculated after excluding the highest and lowest measurements. All experimental data were processed and analyzed using Origin 2024.

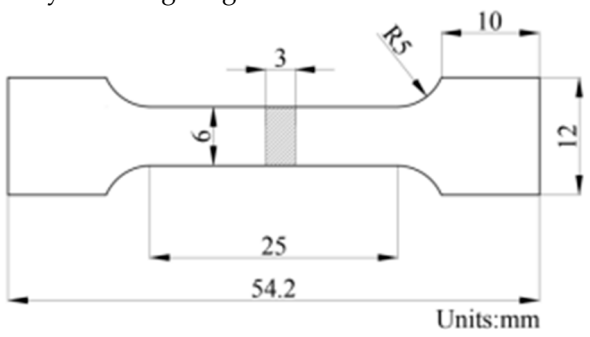
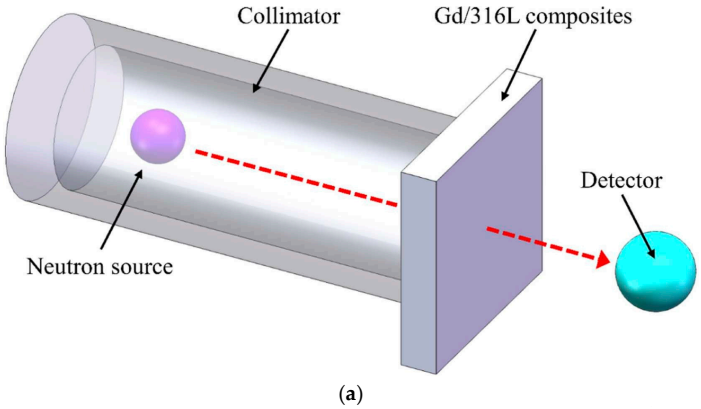


Figure 1. Sample size for tensile test.

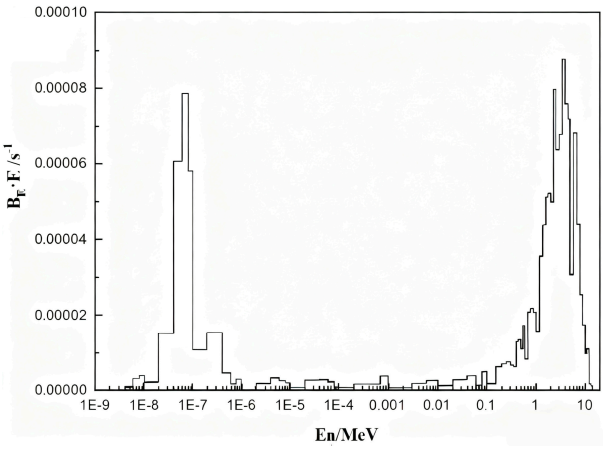
2.4. Neutron Shielding Performance

The neutron shielding performance tests were conducted at the Beijing Radiation Application Research Center. Test samples with dimensions of 150 mm × 150 mm × 6 mm were prepared via wire cutting from as-cast ingots of Mg-12Dy-1Sm-0.4Zr, Mg-12Dy-2Sm-0.4Zr, and Mg-12Dy-3Sm-0.4Zr alloys. A ^{252}Cf neutron source with an emission rate of 8.2×10^7 s^{-1} was used for the neutron shielding evaluation. The source was mounted inside a collimator with an aperture of φ100 mm. A polyethylene moderator placed within the collimator moderated fast neutrons emitted from the ^{252}Cf source. After passing through the collimator, large-angle scattered neutrons were eliminated, resulting in a largely aligned beam of thermal neutrons with energies between 0.01–0.4 eV. Transmitted neutrons through the alloys were detected using a ^{3}He proportional counter. A schematic of the experimental setup and the energy spectrum of the neutron source are shown in Figure 2a,b, respectively.



(**a**)

Figure 2. *Cont.*



(**b**)

Figure 2. (**a**) Schematic diagram of the neutron shielding experiment [29]. Adapted from 'Microstructure, thermophysical properties and neutron shielding properties of Gd/316 L composites for spent nuclear fuel transportation and storage', Materials Today Communications, 1 December 2023, with permission from Elsevier. (**b**) The 252Cf slowed neutron energy spectrum of the experiment [22]. Reprinted from [Le, Y.; et al. Nanotechnol. Rev. 13, 20240007 (2024)], under a CC BY 4.0 license.

The simulations were carried out using Geant4 10.04, an open-source Monte Carlo toolkit widely employed for modeling the interaction and transport of particles through matter. It enables the configuration of diverse physical models to simulate the behavior of various types of particles and their interactions with materials. In cases where experimental studies are infeasible due to high costs or extended durations, alternative approaches such as Geant4 simulations provide an effective means to circumvent experimental limitations, reduce time requirements, and improve the accuracy of results. This toolkit is extensively used across multiple disciplines including high-energy physics, medical applications, nuclear energy, radiation protection, and space science [30]. The simulation model is simplified based on the actual neutron shielding experiments, as shown in Figure 3. The neutron beam emitted by the defined particle gun in the simulation is unidirectional and perpendicular to the alloy, with an energy spectrum referenced from the neutron energy spectrum in Figure 2b. In the simulation, the alloy composition and density are precisely defined, and a virtual uniform material is constructed using the built-in functions in Geant4 based on the specified elemental composition and density. A detector is set up to record the number of neutrons passing through the alloy sample. Additionally, key physical models and processes need to be set in the simulation, including hadronic interactions, neutron capture, neutron scattering, and electromagnetic processes. By comparing the number of neutrons emitted from the neutron source with the number of neutrons detected by the detector after passing through the material, the neutron shielding efficiency and linear attenuation coefficient are obtained.

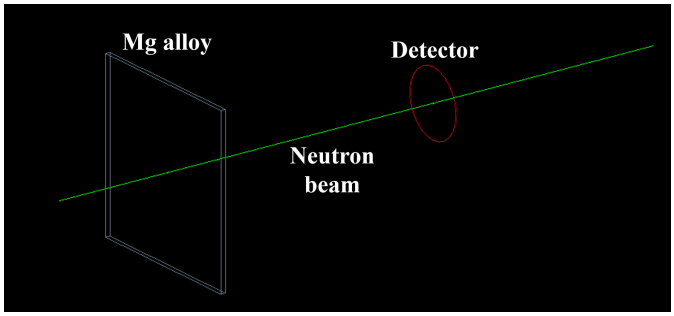


Figure 3. The visualization process of the neutron shielding experiment simulated by Geant4.

3. Results and Discussion

3.1. Microstructure

Figure 4 shows the optical microscopy (OM) images of the Mg-12Dy-xSm-0.4Zr (x = 1, 2, 3) alloys. Bone-like secondary phases can be observed along the grain boundaries, and both the volume fraction and size of these phases increase with higher Sm content. Compared with the microstructure of pure magnesium obtained through the same smelting process, the grains of the magnesium alloy after adding rare earth elements have been significantly refined. This refinement is primarily attributed to the addition of Dy and Sm: a portion of these elements dissolves into the magnesium matrix, strongly inhibiting grain growth during solidification through the constitutional undercooling effect, thereby promoting grain refinement. Another portion continuously segregates during grain growth, accumulating near grain boundaries to form solute-enriched regions. During subsequent cooling, secondary phases precipitate predominantly along these boundaries. These enriched secondary phases effectively pin grain boundaries and hinder grain growth, further contributing to microstructural refinement [31–33]. The addition of Zr also enhances grain refinement. As shown in Figure 5, the grain sizes of all components are not uniform. The average grain sizes of DS1, DS2 and DS3 are 46.33 μm, 52.79 μm and 46.36 μm, respectively. This is mainly due to the fact that nucleation and growth during solidification is a dynamic and random competitive process. Any minor fluctuations in overcooling, solute distribution or thermal conditions can lead to changes in the final grain sizes in different regions. Moreover, as the Sm content increases, more skeletal phases form along the grain boundaries, and their presence also affects the growth of adjacent grains.

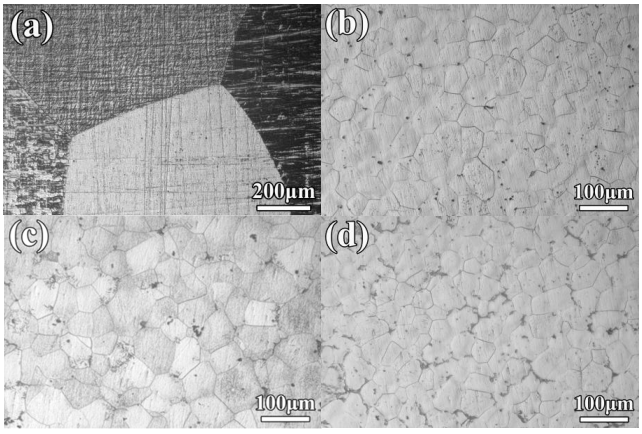


Figure 4. OM of Mg alloys: (**a**) pure Mg, (**b**) DS1, (**c**) DS2, and (**d**) DS3.

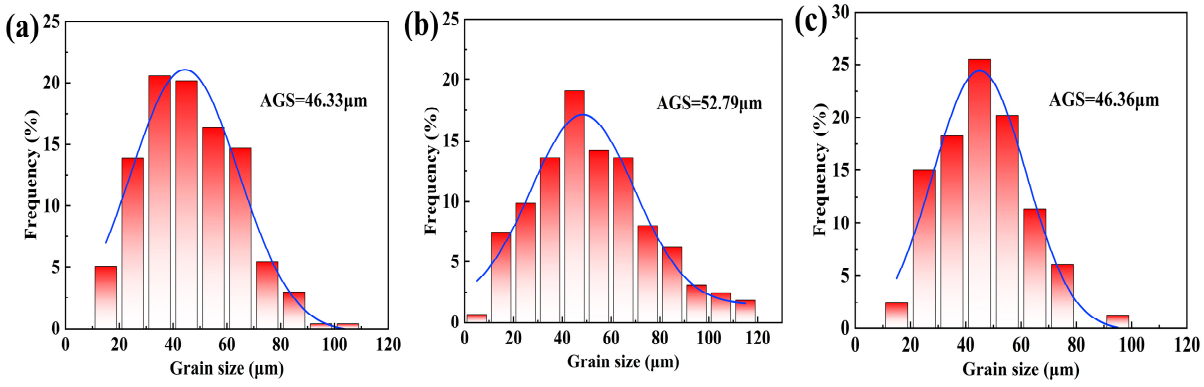


Figure 5. Grain size distribution of Mg alloys: (**a**) DS1, (**b**) DS2, and (**c**) DS3.

Figure 6 below shows the scanning electron microscopy (SEM) images of the Mg-12Dy-xSm-0.4Zr (x = 1, 2, 3) alloys. The maximum solid solubilities of Dy and Sm in magnesium are 25.8% and 5.8%, respectively. In the DS1 alloy (x = 1), no significant bone-like phase is observed along the grain boundaries. Instead, finely dispersed white particulate phases are precipitated within the matrix. Some spherical particles, identified in subsequent analysis as oxide inclusions introduced during the preparation process, are also present. When the Sm content increases to 2% (DS2 alloy), a small number of bone-like phases begin to form along the grain boundaries, though their size remains limited and their quantity is relatively low. With a further increase in Sm content to 3% (DS3 alloy), the bone-like phases exhibit both increased size and quantity, extending continuously along the grain boundaries. In addition, fine blocky particulate phases are segregated within these bone-like structures, as indicated in Figure 6d. The microstructural evolution confirms that Sm is the dominant element governing the formation of the bone-like phase.

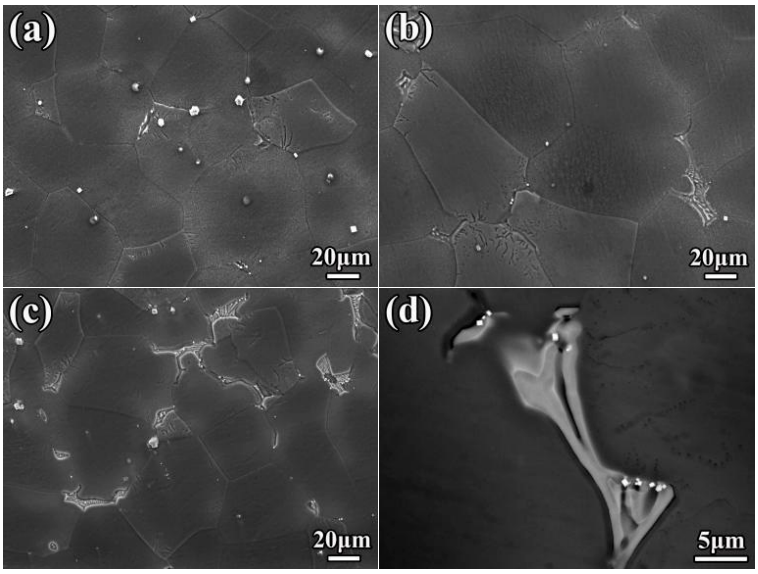


Figure 6. SEM of Mg alloys: (**a**) DS1, (**b**) DS2, (**c**) low-magnification and (**d**) high-magnification views of the DS3 alloy.

Figure 7 presents the XRD spectra of the DS1 and DS3 alloys. The results indicate that, in addition to the α-Mg matrix, the samples primarily contain Mg_5RE phases, Dy-rich phases, and $Mg_{41}Sm_5$ phases, along with trace amounts of impurity phases. Due to the smaller size of the secondary phases compared to the matrix, their diffraction peak intensities are relatively weaker. When the Sm content is 1%, it is difficult to observe secondary phases at the grain boundaries in the microstructure, with only a small amount of particle-like secondary phases dispersed within the matrix. As a result, the peak intensities of Mg_5RE and $Mg_{41}Sm_5$ in the XRD pattern are both weak. Upon comparison of DS1 and DS3, it can be observed that as the Sm content increases, the peak intensities of Mg_5RE and $Mg_{41}Sm_5$ strengthen. The increase in the intensity of the Mg_5RE phase suggests that the addition of Sm promotes the precipitation of the Mg_5RE phase. This is attributed to the fact that Dy, as a Y-group rare earth element, and Sm, as a Ce-group rare earth element, reduce each other's solid solubility in α-Mg, thereby promoting the precipitation of rare earth compounds [34]. Consequently, the number and size of the bone-like secondary phases precipitated at the grain boundaries increase, which results in the enhanced diffraction peaks of Mg_5RE and $Mg_{41}Sm_5$ in the XRD pattern.

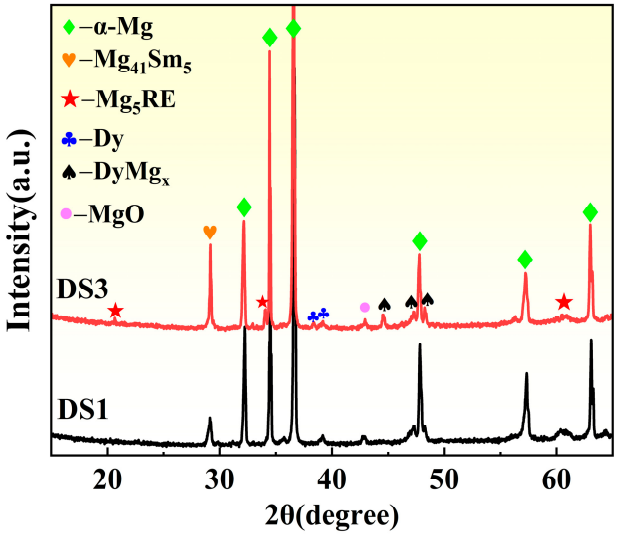


Figure 7. XRD phase analysis of DS1 and DS3.

To further analyze and identify the precipitated phases in the alloys, transmission electron microscopy (TEM) was employed to characterize the composition and structure. Figure 8 shows the STEM results, where significant enrichment of Dy and Sm is observed within the bone-like phase, confirming its rare earth (RE)-rich nature. In addition, partial segregation of Zr was also detected in this phase.

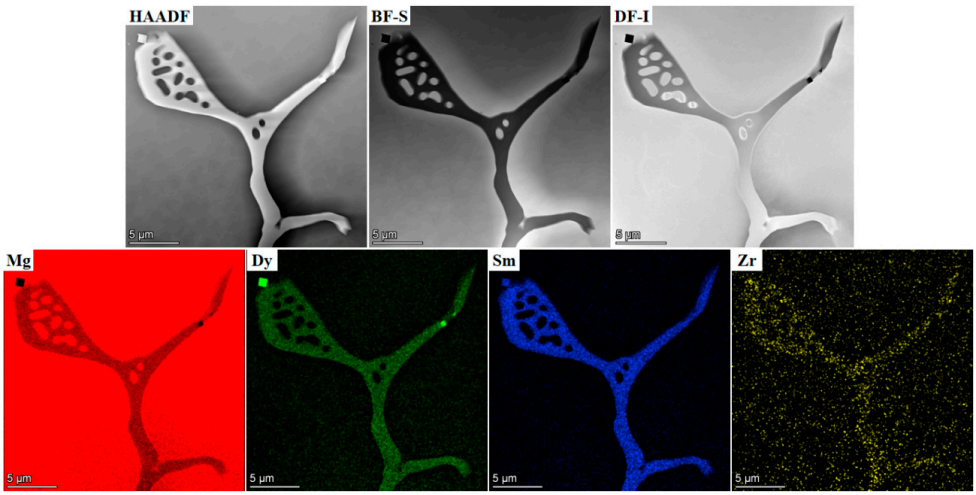


Figure 8. STEM and EDS results of DS3 alloy.

Selected area electron diffraction (SAED) was used to identify the crystal structure of the secondary phases (Figure 9). Micro-area point analysis was conducted within these regions to determine their chemical composition. At point 1, the Mg-to-RE atomic ratio was approximately 5:1, and the corresponding electron diffraction pattern was indexed to a face-centered cubic (FCC) structure. Thus, the bone-like phase was determined to be an FCC-structured Mg_5RE phase with a composition of $Mg_5(Sm_{0.57}Dy_{0.43})$. At point 2, the Dy-to-Sm atomic ratio was about 4:1, and no Mg was detected, suggesting a rare-earth-based secondary phase. At point 3, the Mg-to-Dy atomic ratio was close to 2:1, indicating the presence of an FCC-structured Mg_2Dy phase, in which small amounts of Sm and Zr were dissolved. Composition analysis of the secondary phases reveals that, with the co-addition of Sm and Dy, rare earth elements not only dissolve into the α-Mg matrix but also mutually dissolve into various secondary phases. The $Mg_{41}Sm_5$ phase, though detected by XRD, was not clearly identified in the TEM analysis. Previous studies have indicated that this phase

tends to segregate at grain boundaries and also exhibits a bone-like morphology [35–37]. It is therefore inferred that $Mg_{41}Sm_5$ coexists and mixes with the Mg_5RE phase. Due to its relatively low abundance and morphological similarity, distinguishing it from the Mg_5RE phase under TEM remains challenging.

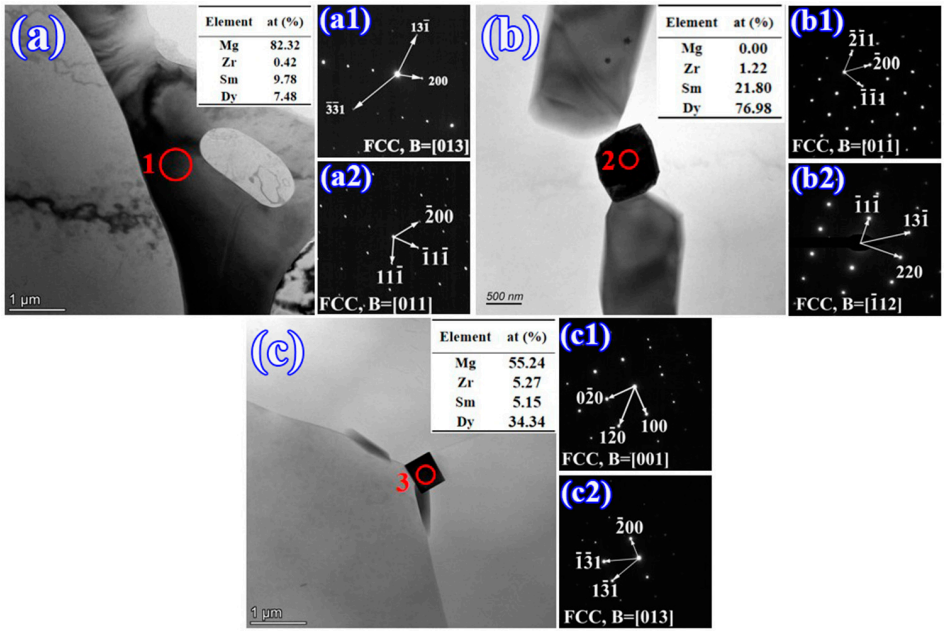


Figure 9. TEM analysis of typical second phases in DS3 alloy: (**a**,**b**,**c**) BF-TEM images and EDS analysis of the marked points; (**a1**,**a2**,**b1**,**b2**,**c1**,**c2**) Corresponding SAED patterns from the points in (**a**,**b**,**c**), respectively.

In summary, the formation of secondary phases results from a competitive precipitation process driven by non-equilibrium solidification and microsegregation. Initially, the addition of Zr, Dy, and Sm refines the α-Mg grains. As solidification progresses, Dy and Sm solute atoms are rejected by α-Mg dendrites, becoming concentrated in inter-dendritic liquid, leading to rare earth-enriched regions along grain boundaries. Local compositional fluctuations in these regions promote a strong supersaturation effect between Dy and Sm [34], causing the preferential nucleation of Mg_5RE-type intermetallic compounds. These phases grow along grain boundaries, forming continuous or semi-continuous networks of $Mg_5(Sm_{0.57}Dy_{0.43})$. In Dy-enriched microzones, the Mg_2Dy phase nucleates once the solute concentration meets precipitation conditions. This phase grows in blocky particles within or along the Mg_5RE network. Rapid cooling locks in this multiphase microstructure, and increasing Sm content further enhances supersaturation at grain boundaries, promoting larger Mg_5RE bone-like phases and more Dy-rich microzones, which leads to a higher density of Mg_2Dy particulate phases within the bone-like structure.

3.2. Mechanical Properties

Figure 10 presents the tensile properties of the as-cast Mg-12Dy-xSm-0.4Zr (x = 1, 2, 3) alloys tested at room temperature, with the corresponding mechanical data summarized in Table 2. For comparison, pure magnesium prepared under the same casting conditions was also tested to exclude potential influences from processing variations. The ultimate tensile strength (UTS), yield strength (YS), and elongation (EL) of cast pure magnesium in this study were measured to be 44.1 MPa, 11.9 MPa, and 7.7%, respectively. These values are slightly lower than those typically reported for cast pure magnesium [38,39]. This can primarily be attributed to differences in the material's melting process. Specifically, the mold preheating temperature for the pure magnesium casting in this study was 400 °C,

which resulted in a slower cooling rate from the melt to room temperature compared to other studies. As a result, the grain size was larger, leading to a slight reduction in strength. The results demonstrate that the co-addition of Dy and Sm significantly enhances both the strength and ductility of the alloys. The ultimate tensile strength reaches up to 194.6 MPa, while the elongation increases to 10.9%, indicating a substantial improvement in the overall mechanical performance due to the incorporation of these rare earth elements. Currently, some reported high rare-earth content cast magnesium alloys, such as the neutron shielding Mg-Gd alloy studied by Le et al., exhibit a yield strength (YS) of 91.7 MPa, an ultimate tensile strength (UTS) of 142.2 MPa, and an elongation (EL) of only 1.8% for the optimally shielding Mg-15Gd as-cast alloy [22]. In the work by Zhu et al. on Mg-16.1Gd-3.5Nd-0.38Zn-0.26Zr-0.15Y alloy, the as-cast properties were YS = 102 MPa, UTS = 122 MPa, and EL = 1.7% [40]. Dai et al. reported that the as-cast Mg-10Gd-3Y-0.8Al alloy achieved YS = 136 MPa, UTS = 215 MPa, and EL = 4.8% [41]. Similarly, Liu et al. studied an as-cast Mg-10Dy-2Sr-Nd-Zr alloy with YS = 105 MPa, UTS = 166 MPa, and EL = 6.4% [42]. In comparison, the mechanical properties of the Mg-Dy-Sm-Zr alloy developed in this study are either superior or comparable to those reported in the literature.

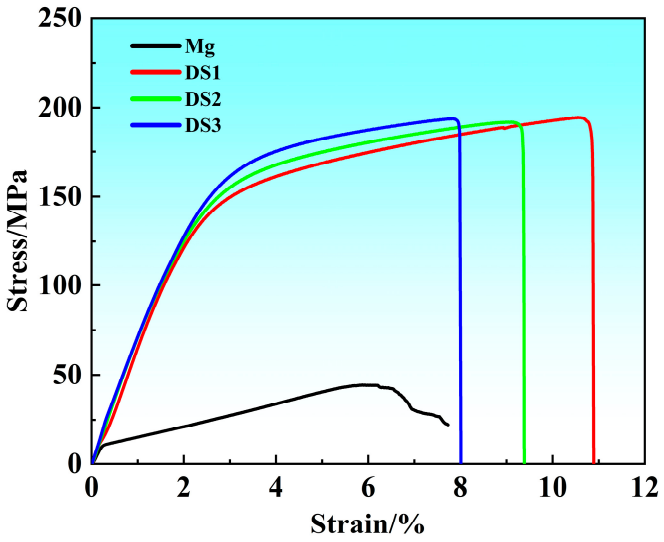


Figure 10. The stress–strain curve of Mg-12Dy-xSm-0.4Zr alloy.

Table 2. Test results of mechanical properties of Mg-12Dy-xSm-0.4Zr alloy.

Sample	UTS (MPa)	YS (MPa)	EL (%)
Mg	44.1	11.9	7.7
Mg-12Dy-1Sm-0.4Zr	194.6	138.2	10.9
Mg-12Dy-2Sm-0.4Zr	191.9	128.0	9.4
Mg-12Dy-3Sm-0.4Zr	193.4	125.9	8.0

With increasing Sm content, the ultimate tensile strength (UTS) of the alloys did not change significantly, but both the yield strength and elongation gradually decreased. This indicates that beyond a certain threshold, the addition of Sm may adversely affect ductility. The strengthening mechanisms in magnesium alloys primarily include solid solution strengthening, grain refinement strengthening, and secondary phase strengthening [43]. In the present alloy system, the improvement in strength can be attributed to the synergistic effects of multiple strengthening mechanisms induced by the combined addition of rare earth elements (Dy, Sm) and Zr. First, grain refinement plays a key role. Under non-equilibrium cooling conditions, undissolved particles and precipitates containing RE and Zr can act as heterogeneous nucleation sites for α-Mg grains, promoting refinement.

Meanwhile, both RE and Zr induce pronounced constitutional supercooling ahead of the solid/liquid interface, suppressing dendritic growth and further refining the grain structure. This contributes to enhanced strength and improved plasticity [44]. Second, solid solution strengthening is another important factor. Dysprosium (Dy) exhibits high solid solubility in magnesium and can dissolve extensively into the matrix under rapid cooling conditions, causing lattice distortion and effectively hindering dislocation motion [45], thereby increasing alloy strength. Samarium (Sm) can also partially dissolve into the matrix during non-equilibrium solidification, further contributing to solid solution strengthening. Third, secondary phase strengthening is significant. Sm tends to precipitate at grain boundaries, forming bone-like secondary phases (Mg_5RE, $Mg_{41}Sm_5$) distributed along the boundaries. These phases can effectively pin grain boundaries and dislocations, inhibiting boundary migration and slip, thus enhancing strength [46]. However, when the Sm content exceeds a certain level, excessive secondary phases accumulate at the grain boundaries, causing intergranular embrittlement. During tensile deformation, these phases act as stress concentration sites, promoting the initiation of internal microcracks, which can serve as crack initiation points or act as propagation paths for other cracks, resulting in a decrease in yield strength and plasticity. This observation is consistent with findings reported by Zhou et al. [36], confirming the critical influence of the morphology and distribution of secondary phases on mechanical properties at higher Sm contents.

Figure 11 shows the micro-Vickers hardness test results of the alloy series. As the Sm content increases, the average hardness of the alloys continuously rises. This is mainly attributed to the combined effects of the following factors: increased solute atom content in the solid solution leading to enhanced lattice distortion and greater impediment to dislocation movement; grain refinement effects contributed by Zr and rare earth elements; and the obstruction of matrix deformation by secondary phases formed through rare earth additions. The synergy of these multiple strengthening mechanisms significantly improves the overall hardness of the alloys.

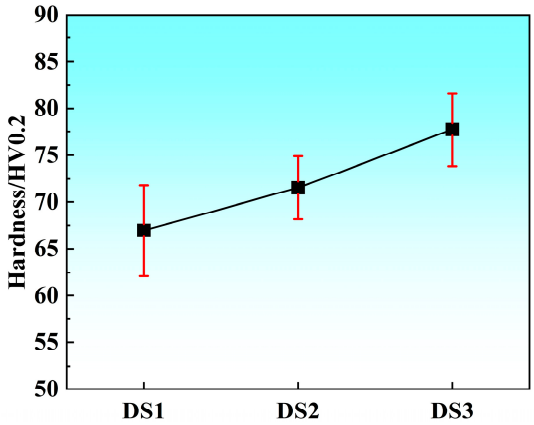


Figure 11. The micro-Vickers hardness of Mg-12Dy-xSm-0.4Zr alloy.

3.3. Fracture Behavior

Figure 12 presents the tensile fracture morphologies of the Mg-12Dy-xSm-0.4Zr alloys, revealing a typical quasi-cleavage fracture mechanism. As shown in Figure 12(a1,b1,c1), the fracture surfaces exhibit mixed morphological features, including cleavage planes, tear ridges, and a small number of dimples. The smooth and flat cleavage planes correspond to the rapid propagation of cracks along specific crystallographic planes. The raised tear ridges are formed by localized plastic tearing between cleavage planes at different heights. The presence of fine dimples in localized regions indicates limited plastic deformation prior to fracture [47]. Further observation of the magnified bone-shaped secondary phase in Figure 12(a2,b2,c2) reveals obvious microcracks within this phase. Combined with previous

analysis, this phase is primarily composed of hard and brittle intermetallic compounds such as Mg_5(Sm,Dy), enriched with Dy and Sm, and distributed along grain boundaries. Under tensile stress, due to its high brittleness and poor deformation compatibility with the matrix, this phase is prone to form microcracks during the early stages of deformation. These microcracks act as "pre-existing crack sources", significantly reducing the energy barrier for crack initiation. Moreover, when propagating main cracks encounter these bone-shaped phases containing microcracks, they rapidly connect and coalesce, greatly accelerating the crack propagation process and leading to early brittle fracture of the material. As the Sm content increases from 1 wt% to 3 wt%, the quantity and size of the bone-shaped secondary phase in the alloy increase significantly, and its continuous network distribution becomes more pronounced. This not only increases the number of potential crack sources but also provides more low-resistance paths for crack propagation, thereby further reducing both the yield strength and elongation.

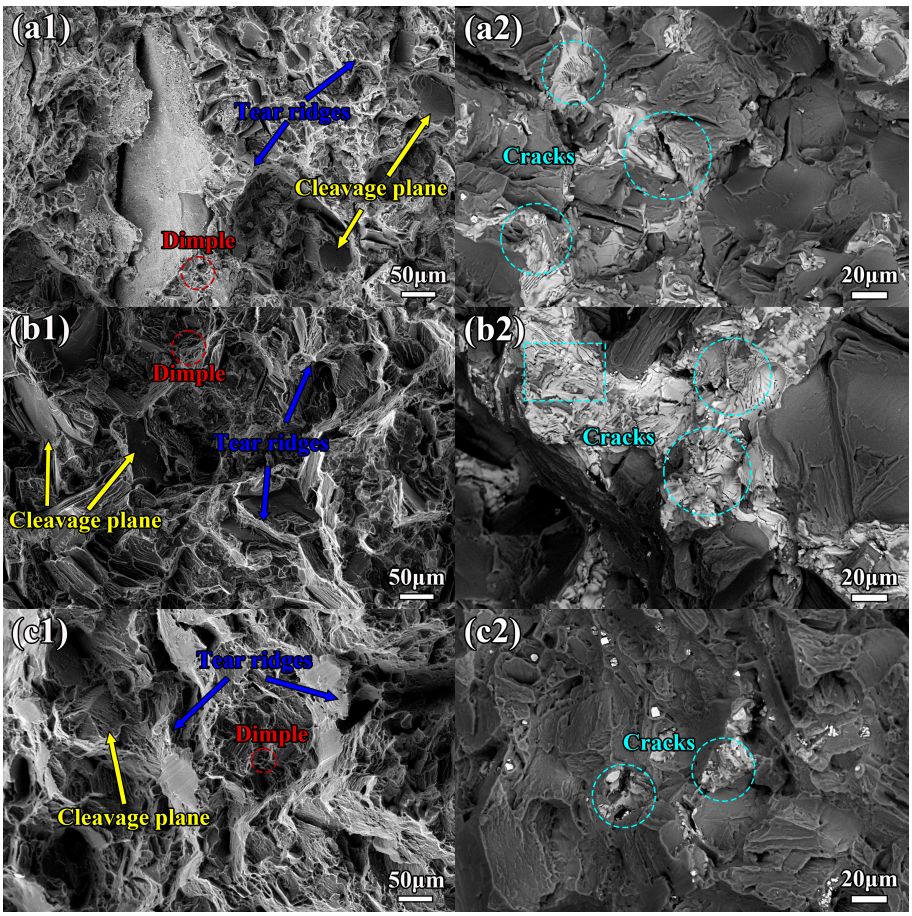


Figure 12. The tensile fracture morphology of the alloy: (**a1**,**a2**) DS1, (**b1**,**b2**) DS2 and (**c1**,**c2**) DS3.

Therefore, the morphology, distribution, and internal microcracking behavior of the bone-shaped secondary phase are key microstructural factors affecting the strength-ductility balance in this alloy series. Subsequent optimization of the microstructure distribution can be achieved through appropriate heat treatment processes, such as solution treatment, aging treatment, or a combination of both, which has been supported by existing research on Mg–RE alloys. For instance, Xu et al. investigated the effect of heat treatment on the Mg-11.46Gd-4.08Y-2.09Zn-0.56Zr alloy and found that T5 and T6 heat treatments improved microstructural homogeneity, reduced residual stress, precipitated fine and uniformly distributed β′ phases with strengthening effects [48]. Zeng et al. performed a solution treatment at 520 °C for 20 h on the Mg–12.23Dy–2.55Nd–0.4Zr alloy, which resulted in

the dissolution of most eutectic phases at grain boundaries into the matrix, leaving only some particulate phases and significantly improving the quantity and distribution of the secondary phases [49]. Wu et al. applied a solution treatment at 500 °C for 10 h followed by aging at 200 °C for 20 h to a Mg-Nd-Zn-Zr alloy prepared by the WADED process. During this heat treatment, the intergranular eutectic phase dissolved, and fine γ_1 and β'reinforcing phases precipitated, improving the synergy between strength and toughness of the alloy [50]. Similarly, Yi et al. studied the Mg-2.0Sm-0.4Zn-0.4Zr-2.5Nd alloy and found that solution treatment at 515 °C for 8 h dissolved the coarse β eutectic phase, while the subsequent aging treatment at 200 °C for 18 h promoted the formation of nanoscale precipitates, doubling the tensile strength in the aged state compared to the as-cast state [51]. Therefore, a customized solution and aging treatment process can be applied to the Mg-Dy-Sm-Zr alloy in this study, which may help reduce the continuous bone-shaped phase and induce the precipitation of fine, densely distributed nanoscale precipitates in the matrix, thereby improving both strength and ductility.

3.4. Neutron Shielding Performance

The process by which rare earth elements undergo neutron capture reactions (Figure 13) consists mainly of two stages: capture and de-excitation. First, the nucleus of a rare earth atom captures a thermal neutron (low-energy neutron), forming a compound nucleus in an excited state. Subsequently, this compound nucleus de-excites to a stable ground state by emitting one or multiple high-energy photons (γ-rays). The emitted γ-rays are referred to as "secondary γ-rays" or "capture γ-rays". The neutron absorption cross-section (σ) is a physical quantity that characterizes the probability of an interaction occurring between an atomic nucleus and a neutron. It can be understood as the effective cross-sectional area of the nucleus acting as a "target". A larger cross-section indicates a higher probability of a reaction occurring between the neutron and the nucleus. Therefore, in traditional boron-containing neutron shielding materials—whether metal-based or polymer-based—shielding performance relies on the high neutron absorption cross-section of ^{10}B. However, the neutron reaction with ^{10}B (n, α) [52]:

$$^{10}_{5}\mathrm{B} + ^{1}_{0}\mathrm{n} \rightarrow ^{7}_{3}\mathrm{Li}(1.015\ \mathrm{MeV}) + \alpha(1.777\ \mathrm{MeV})6\%$$

$$^{10}_{5}\mathrm{B} + ^{1}_{0}\mathrm{n} \rightarrow ^{7}_{3}\mathrm{Li}^{*}(0.840\ \mathrm{MeV}) + \alpha(1.470\ \mathrm{MeV})94\%$$

Although this reaction effectively absorbs neutrons, the resulting Li ions and He bubbles can easily lead to material irradiation swelling, microcracking, and degradation of mechanical properties [53]. Moreover, the transmutation product of boron after neutron absorption, ^{11}B, exhibits a drastically reduced neutron absorption cross-section, resulting in significantly diminished neutron shielding performance [54].

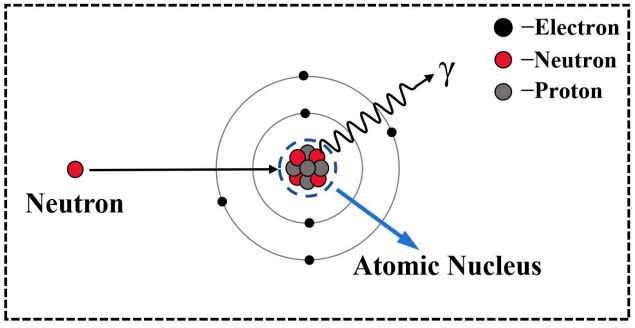


Figure 13. Schematic diagram of the neutron capture reaction.

Among rare earth elements, gadolinium (Gd) is generally regarded as the most effective neutron absorber, with a thermal neutron absorption cross-section as high as 48,800 barns. However, after capturing a neutron, Gd undergoes an (n, γ) reaction and releases multiple high-energy secondary γ-rays (with a total energy spectrum reaching up to 7.9 MeV or higher) [55]:

$$^{155}_{64}\mathrm{Gd} + ^{1}_{0}\mathrm{n} \rightarrow ^{156}_{64}\mathrm{Gd} + \mathrm{RP}(8.54\ \mathrm{MeV})$$

$$^{157}_{64}\mathrm{Gd} + ^{1}_{0}\mathrm{n} \rightarrow ^{158}_{64}\mathrm{Gd} + \mathrm{RP}(7.94\ \mathrm{MeV})$$

RP is mainly secondary gamma rays. These high-energy secondary gamma rays have extremely strong penetrating power and require heavy elements (such as lead and tungsten) for shielding [56], thereby increasing the weight and structural complexity of the shielding system—an outcome undesirable for lightweight applications. In contrast, the Sm and Dy elements introduced in this study also exhibit high thermal neutron absorption cross-sections (^{149}Sm: 40,080 barns; ^{164}Dy: 2650 barns). Their neutron capture reactions are also predominantly (n, γ) reactions

$$^{149}_{62}\mathrm{Sm} + ^{1}_{0}\mathrm{n} \rightarrow ^{150}_{62}\mathrm{Sm} + \mathrm{RP}$$

$$^{164}_{66}\mathrm{Dy} + ^{1}_{0}\mathrm{n} \rightarrow ^{165}_{66}\mathrm{Dy} + \mathrm{RP}$$

Figure 14 presents the experimental and simulated results of the thermal neutron shielding rate and linear attenuation coefficient for samples with dimensions of 150 mm × 150 mm × 6 mm. Denoting the number of incident neutrons as N_0 and the number of neutrons recorded by the detector as N_1, the shielding rate is calculated as follows:

$$\text{Shielding rate} = \left[\frac{(N_0 - N_1)}{N_0}\right] \times 100\%$$

The linear attenuation coefficient μ represents the proportion by which the intensity of a neutron beam is reduced per unit thickness of the material. A higher value of μ indicates that neutrons attenuate more rapidly within the material, reflecting better shielding performance per unit thickness. The coefficient μ satisfies the following relationship:

$$I = I_0 e^{-\mu x}$$

where I_0 is the initial intensity of the incident neutron beam, and I is the intensity after the beam has passed through a material of thickness "x". Under identical experimental conditions, N_0 and N_1 can be approximated as proportional to I_0 and I, respectively.

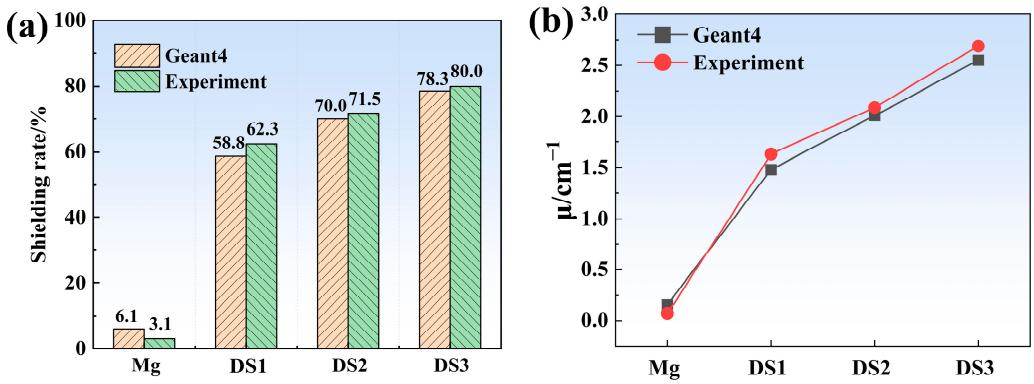


Figure 14. (**a**) The shielding rate of the alloy against thermal neutrons, (**b**) the linear attenuation coefficient of the alloy.

Both experimental and simulation (Geant4) results indicate that as the Sm content increases, the neutron shielding rate and linear attenuation coefficient of the alloys improve significantly, with consistent trends observed between the two methods. The difference between the experimental values and the simulated values is small, which mutually verifies the reliability of the results. Compared with pure magnesium, the addition of Dy and Sm greatly enhances the thermal neutron absorption performance of the alloys. The improvement in neutron shielding capacity can be attributed to two main factors: (1) Compared to pure magnesium, Sm and Dy have larger thermal neutron absorption cross-sections. The incorporation of these effective neutron-absorbing elements increases the macroscopic absorption cross-section of the material, enhancing the capture of thermal neutrons. (2) The microstructure of the magnesium alloy also influences its neutron shielding performance. Microstructural optimization through grain refinement and precipitation of secondary phases improves shielding efficiency: the rare earth-rich phases become more uniformly distributed with reduced inter-particle spacing, thereby shortening the mean free path of neutrons. A shorter mean free path means that within the same material thickness, neutrons have a higher probability of interacting with atomic nuclei, leading to more effective absorption over shorter distances and increasing the likelihood of interaction with absorbing elements [22].

A key advantage lies in the fact that the secondary γ-rays produced after thermal neutron capture by Sm and Dy have relatively low energy, making them easier to absorb by the shielding material itself or by thinner additional shielding layers. Moreover, the transmutation products generated after neutron absorption maintain sustained neutron absorption capability [23,25]. Additionally, Dy and Sm, being high atomic number (Z) elements, can also absorb γ-rays during the shielding process [16]. Furthermore, since the (n, γ) reaction does not produce gaseous products such as helium or hydrogen, it avoids issues like material swelling, microcracking, and mechanical degradation caused by the accumulation of helium bubbles, thereby ensuring better long-term irradiation stability.

It should be noted that the discrepancies between simulated and experimental values are primarily due to the ideal conditions assumed in the simulations (such as uniform element distribution and monoenergetic neutron beam incidence), whereas real-world conditions—including neutron reflection, scattering, and compositional segregation (e.g., aggregation of secondary phases at grain boundaries)—affect the actual experimental results. Nevertheless, the simulations effectively predict the experimental trends, providing a reliable reference for subsequent compositional optimization.

4. Conclusions

The microstructure, mechanical properties, and thermal neutron shielding properties of as-cast Mg-12Dy-xSm-0.4Zr (x = 1, 2, 3 wt%) alloys were investigated. The results indicate that the combined addition of Dy, Sm, and Zr significantly refined the α-Mg grains. The microstructure consists primarily of an α-Mg matrix and various rare-earth (RE) phases. The amount and size of these RE phases increased with higher Sm content. Compared to pure magnesium, the alloy's strength and elongation were significantly improved, with ultimate tensile strength (UTS) reaching up to 194.6 MPa and elongation (EL) reaching 10.9%. However, the increase in Sm content led to coarsening of the second phases, resulting in a decrease in both yield strength (YS) and elongation (EL). The addition of Dy and Sm markedly enhanced the thermal neutron shielding capacity of the alloys. Both the shielding rate and linear attenuation coefficient increased with higher Sm content, which is primarily attributed to the large thermal neutron absorption cross-sections of Sm and Dy, as well as the refined microstructure that shortens the mean free path of neutrons. In summary,

the alloy exhibits promising overall performance and shows potential for application in neutron shielding materials.

Author Contributions: Conceptualization, J.S. and W.Z.; Methodology, H.L., J.S. and W.Z.; Investigation, H.L., C.D. and E.N.; Data Curation, H.L., X.X. and C.D.; Writing—Original Draft Preparation, H.L.; Writing—Review & Editing, J.S., J.T., W.Z. and J.M.; Project Administration, J.S., X.X. and W.Z.; Funding Acquisition, J.S. and W.Z. All authors have read and agreed to the published version of the manuscript.

Funding: This research was funded by National Science and Technology Major Project and Academician in Key Research and Development Plan of Sichuan Province (2024YFHZ0118).

Data Availability Statement: The original contributions presented in this study are included in the article. Further inquiries can be directed to the corresponding authors.

Conflicts of Interest: The authors declare no conflicts of interest.

References

1. Addo, E.K.; Kabo-bah, A.T.; Diawuo, F.A.; Debrah, S.K. The Role of Nuclear Energy in Reducing Greenhouse Gas (GHG) Emissions and Energy Security: A Systematic Review. *Int. J. Energy Res.* **2023**, *2023*, 8823507. [CrossRef]
2. Chen, J.; Zhang, X.; Xiao, W.; Pan, D.; Wu, W. Advances in Gadolinium-Based Composite Materials for Neutron and Gamma-Ray Shielding. *Front. Mater.* **2025**, *12*, 1561198. [CrossRef]
3. Gan, B.; Liu, S.; He, Z.; Chen, F.; Niu, H.; Cheng, J.; Tan, B.; Yu, B. Research Progress of Metal-Based Shielding Materials for Neutron and Gamma Rays. *Acta Metall. Sin.-Engl. Lett.* **2021**, *34*, 1609–1617. [CrossRef]
4. Bakri, F.; Gareso, P.L.; Armynah, B.; Tahir, D. A Comparative Study of Glass-Based Material Counter to X-Ray, Gamma-Ray, and Proton and Neutron Radiation: A Review. *Radiat. Phys. Chem.* **2025**, *226*, 112270. [CrossRef]
5. Hao, Z.; Gong, J.; Liang, C. Polymer-Based Neutron Shielding Materials: A Critical Review on Application-Specific Performance Trade-Offs and Optimization Strategies. *Polym. Compos.* **2025**, *early view*.
6. Piotrowski, T. Neutron Shielding Evaluation of Concretes and Mortars: A Review. *Constr. Build. Mater.* **2021**, *277*, 122238. [CrossRef]
7. Yilmaz, D.; Aktas, B.; Calik, A.; Aytar, O.B. Boronizing Effect on the Radiation Shielding Properties of Hardox 450 and Hardox HiTuf Steels. *Radiat. Phys. Chem.* **2019**, *161*, 55–59. [CrossRef]
8. Zhang, P.; Li, Y.; Wang, W.; Gao, Z.; Wang, B. The Design, Fabrication and Properties of B4C/Al Neutron Absorbers. *J. Nucl. Mater.* **2013**, *437*, 350–358. [CrossRef]
9. Arslan, G.; Kara, F.; Turan, S. Quantitative X-Ray Diffraction Analysis of Reactive Infiltrated Boron Carbide–Aluminium Composites. *J. Eur. Ceram. Soc.* **2003**, *23*, 1243–1255. [CrossRef]
10. Fu, X.; Ji, Z.; Lin, W.; Yu, Y.; Wu, T. The Advancement of Neutron Shielding Materials for the Storage of Spent Nuclear Fuel. *Sci. Technol. Nucl. Install.* **2021**, *2021*, 5541047. [CrossRef]
11. Tasnim, A.; Sahadath, M.H.; Khan, M.N.I. Development of High-Density Radiation Shielding Materials Containing $BaSO_4$ and Investigation of the Gamma-Ray Attenuation Properties. *Radiat. Phys. Chem.* **2021**, *189*, 109772. [CrossRef]
12. Singh, P.; Kaur, G.; Kumar, R.; Kumar, U.; Singh, K.; Kumar, M.; Bala, R.; Meena, R.; Kumar, A. Boron Carbide Nanostructures: A Prospective Material as an Additive in Concrete. In Proceedings of the 2nd International Conference on Condensed Matter and Applied Physics (ICC), Bikaner, India, 24–25 November 2017; AIP Publishing: Melville, NY, USA, 2018; p. 030278.
13. Pan, F.; Yang, M.; Chen, X. A Review on Casting Magnesium Alloys: Modification of Commercial Alloys and Development of New Alloys. *J. Mater. Sci. Technol.* **2016**, *32*, 1211–1221. [CrossRef]
14. Mounier, C. Thermal Neutron Cross-Sections of Magnesium. *Ann. Nucl. Energy* **2004**, *31*, 911–921. [CrossRef]
15. Jing, H.; Geng, L.; Qiu, S.; Zou, H.; Liang, M.; Deng, D. Research Progress of Rare Earth Composite Shielding Materials. *J. Rare Earths* **2023**, *41*, 32–41. [CrossRef]
16. Lu, Y.; Huo, Z.; Zhong, G.; Zhang, H.; Hu, L. Rare Earth Based Neutron and Gamma Composite Shielding Materials. *Prog. Chem.* **2023**, *35*, 1214–1228.
17. Hossain, M.K.; Raihan, G.A.; Akbar, M.A.; Kabir Rubel, M.H.; Ahmed, M.H.; Khan, M.I.; Hossain, S.; Sen, S.K.; Jalal, M.I.E.; El-Denglawey, A. Current Applications and Future Potential of Rare Earth Oxides in Sustainable Nuclear, Radiation, and Energy Devices: A Review. *ACS Appl. Electron. Mater.* **2022**, *4*, 3327–3353. [CrossRef]
18. Vinothkumar, P.; Mohapatra, M.; Dhavamurthy, M.; Murugasen, P.; Suresh, A.A. The Effect of Rare Earth on the Radiation Shielding Properties of Transparent Lead-Free Alumino-Borophosphate Glass System. *Radiat. Phys. Chem.* **2022**, *193*, 109941.

19. Wang, K.; Ma, L.; Yang, C.; Bian, Z.; Zhang, D.; Cui, S.; Wang, M.; Chen, Z.; Li, X. Recent Progress in Gd-Containing Materials for Neutron Shielding Applications: A Review. *Materials* **2023**, *16*, 4305. [CrossRef]
20. Wu, G.; Wang, C.; Sun, M.; Ding, W. Recent Developments and Applications on High-Performance Cast Magnesium Rare-Earth Alloys. *J. Magnes. Alloys* **2021**, *9*, 1–20. [CrossRef]
21. You, S.; Huang, Y.; Kainer, K.U.; Hort, N. Recent Research and Developments on Wrought Magnesium Alloys. *J. Magnes. Alloys* **2017**, *5*, 239–253. [CrossRef]
22. Le, Y.; She, J.; Mao, J.; Jing, X.; Yang, J.; Meng, X.; Tan, J.; Wu, L.; Zhang, W.; Yang, W.; et al. Novel Integrated Structure and Function of Mg-Gd Neutron Shielding Materials. *Nanotechnol. Rev.* **2024**, *13*, 20240007. [CrossRef]
23. Gaylan, Y.; Dag, I.E.; Caglar, S.; Avar, B. Investigation of Mechanical and Radiation Shielding Properties of Sm-Sm_2O_3 Reinforced Al-B4C Composite. *Radiat. Phys. Chem.* **2025**, *226*, 112325. [CrossRef]
24. Zeng, Z.; Pan, H.; Pan, Z.; Wang, S.; Huang, Y.; Tang, W.; Yang, C.; Ren, Y.; Qin, G. Effect of Sm and Ce Content on Microstructure and Mechanical Property of Newly Developed Mg-Sm-Ce-Mn Based Alloy. *Mater. Charact.* **2023**, *206*, 113420. [CrossRef]
25. Pan, J.; Liu, A.; Wang, C.; Li, J.; Wu, Z.; Xiao, X. Fabrication and Characterization of Novel High-Efficiency and High-Durability Neutron-Absorbing Ni-Based Alloys. *Nucl. Mater. Energy* **2024**, *41*, 101768. [CrossRef]
26. An, R.; Cao, J.; Su, X.; Feng, Z.; Li, Y.; Li, Z.; Xiong, J. Research Status of Microstructure and Mechanical Properties of Cast Magnesium Alloys Containing Dy. *Spec. Cast Nonferrous Alloys* **2021**, *41*, 1374–1380.
27. Li, S.; Du, W.; Wang, X.; Li, J.; Wu, Z.; Xiao, X. Effect of Zr Addition on the Grain Refinement Mechanism of Mg-Gd-Er Alloys. *Acta Metall. Sin.* **2018**, *54*, 911–917.
28. Sun, M.; Yang, D.; Zhang, Y.; Mao, L.; Li, X.; Pang, S. Recent Advances in the Grain Refinement Effects of Zr on Mg Alloys: A Review. *Metals* **2022**, *12*, 1388. [CrossRef]
29. Qi, Z.; Yang, Z.; Meng, X.; Yang, X.; Liang, M.; Li, C.; Dai, Y. Microstructure, Thermophysical Properties and Neutron Shielding Properties of Gd/316 L Composites for Spent Nuclear Fuel Transportation and Storage. *Mater. Today Commun.* **2023**, *37*, 107315. [CrossRef]
30. Al-Buriahi, M.S.; El-Agawany, F.I.; Sriwunkum, C.; Akyildirim, H.; Arslan, H.; Tonguc, B.T.; El-Mallawany, R.; Rammah, Y.S. Influence of Bi_2O_3/PbO on Nuclear Shielding Characteristics of Lead-Zinc-Tellurite Glasses. *Phys. B Condens. Matter* **2020**, *581*, 411946. [CrossRef]
31. Shi, H.; He, J.; Wen, J.; Li, H.; Xu, D.; Liu, Q. Effect of Rare Earth Element Dy on Microstructure and Properties of Mg-2Zn-0.5Zr Bio-Magnesium Alloy. *Mater. Heat Treat.* **2020**, *41*, 12–18.
32. Xie, J.; Zhang, J.; You, Z.; Liu, S.; Guan, K.; Wu, R.; Wang, J.; Feng, J. Towards Developing Mg Alloys with Simultaneously Improved Strength and Corrosion Resistance via RE Alloying. *J. Magnes. Alloys* **2021**, *9*, 41–56. [CrossRef]
33. Yu, M.; Guo, E.; Feng, Y.; Wang, L.; Wang, C. Effect of Sm on Microstructure and Mechanical Properties of As-Cast Mg-0.4Zn-0.8Zr Alloys. *Heat Treat. Met.* **2016**, *41*, 78–80.
34. Zhu, L.; Li, Q.; Zhou, Y.; Yan, J. Effect of Sm on Microstructures and Mechanical Properties of Mg-10Gd-0.5Zr Alloy. *Rare Met. Mater. Eng.* **2019**, *48*, 171–176.
35. Yuan, M.; He, C.; Dong, Z.; Jiang, B.; Song, B.; Guo, N.; Liu, T.; Guo, S.; Pan, F. Effect of Sm Addition on the Microstructure and Mechanical Properties of Mg-xSm-0.4Zr Alloys. *J. Mater. Res. Technol.* **2023**, *23*, 4814–4827. [CrossRef]
36. Zhou, Y.; Li, Q.; Fu, S.; Zhang, X.; Cheng, X.; Yan, J. Microstructure and Properties Analysis of As Cast Mg-11Gd-2Y-xSm-0.5Zr Alloy. *Foundry* **2017**, *66*, 178–181.
37. Zhang, Z. Study on the Microstructure, Mechanical Properties and Precipitation Phase Transformation in Mg(-Gd)-Sm-Zr Alloy. Ph.D. Thesis, Shanghai Jiao Tong University, Shanghai, China, 2009.
38. Lei, W.; Wang, H.; Liang, W. Microstructure and Mechanical Properties of Pure Magnesium Subjected to Hot Extrusion. *J. Wuhan Univ. Technol. Mater. Sci. Ed.* **2019**, *34*, 1193–1196. [CrossRef]
39. Jamel, M.; Lopez, H.; Schultz, B.; Otieno, W. The Effect of Solidification Rate on the Microstructure and Mechanical Properties of Pure Magnesium. *Metals* **2021**, *11*, 1264. [CrossRef]
40. Zhu, X.; Yao, J.; Wu, H.; Liu, X.; Liu, H.; Fan, Z.; Lv, S.; Wang, K.; Wang, Z. Microstructure and Mechanical Properties of a Cast Heat-Resistant Rare-Earth Magnesium Alloy. *China Foundry* **2023**, *20*, 289–298. [CrossRef]
41. Dai, J.; Zhu, S.; Easton, M.A.; Zhang, M.; Qiu, D.; Wu, G.; Liu, W.; Ding, W. Heat treatment, microstructure and mechanical properties of a Mg–Gd–Y alloy grain-refined by Al additions. *Mater. Sci. Eng. A* **2013**, *576*, 298–305. [CrossRef]
42. Liu, D.; Yin, X.; Pang, X.; Hu, S.; Ding, Y. Effects of Dy, Sr and Die Casting on Microstructure, Mechanical and Corrosion Properties of Mg-Dy-Sr-Nd-Zr Alloys. *J. Mater. Eng. Perform.* **2017**, *26*, 3983–3992. [CrossRef]
43. Li, Z.; Xu, M.; Cao, Y.; Zhao, Y. Current Progress in Strengthening, Plastic Deformation and Thermal Stability of Mg Alloys. *J. Alloys Compd.* **2025**, *1018*, 179151. [CrossRef]
44. Wu, G.; Tong, X.; Jiang, R.; Ding, W. Grain Refinement of As-Cast Mg-RE Alloys: Research Progress and Future Prospect. *Acta Metall. Sin.* **2022**, *58*, 385–399.

45. Yang, L.; Huang, Y.; Peng, Q.; Feyerabend, F.; Kainer, K.U.; Willumeit, R.; Hort, N. Mechanical and Corrosion Properties of Binary Mg-Dy Alloys for Medical Applications. *Mater. Sci. Eng. B* **2011**, *176*, 1827–1834. [CrossRef]
46. Bao, J.; Li, Q.; Chen, X.; Zhang, Q.; Chen, Z. Microstructure and Texture Evolution with Sm Addition in Extruded Mg-Gd-Sm-Zr Alloy. *Mater. Res. Express* **2021**, *8*, 096523. [CrossRef]
47. Karparvarfard, S.M.H.; Shaha, S.K.; Behravesh, S.B.; Jahed, H.; Williams, B. Microstructure, Texture and Mechanical Behavior Characterization of Hot Forged Cast ZK60 Magnesium Alloy. *J. Mater. Sci. Technol.* **2017**, *33*, 907–918. [CrossRef]
48. Xu, H.; Li, Y.; Wu, L.; Jiang, F.; Fu, D.; Teng, J.; Zhang, H. Effect of Heat Treatments on the Corrosion Resistance of a High Strength Mg-Gd-Y-Zn-Zr Alloy. *Materials* **2022**, *15*, 2813. [CrossRef]
49. Zeng, X.Q.; Li, D.H.; Dong, J.; Lu, C.; Ding, W. Effect of Solution Treatment and Extrusion on Evolution of Microstructure in a Mg-12Dy-3Nd-0.4Zr Alloy. *J. Alloys Compd.* **2008**, *456*, 419–424. [CrossRef]
50. Wu, K.; Zhang, X.; Wang, W.; Shen, F.; Zheng, X.; Wei, X.; Liang, J.; Liang, X.; Zhu, D.; Zhang, Z. Enhanced Strength-Ductility Synergy of Mg-Nd-Zn-Zr Alloys Fabricated by Wire-Arc Directed Energy Deposition and Subsequent Heat Treatment. *J. Alloys Compd.* **2025**, *1036*, 181999. [CrossRef]
51. Yi, S.; Zhao, S.; Feng, Y.; Wang, L.; Guo, E.; Sun, Q. Effect of Heat Treatment on Microstructure, Mechanical Properties and Corrosion Behavior of Mg-Sm-Zn-Zr-xNd Alloys. *J. Mater. Res. Technol.* **2025**, *36*, 5341–5354. [CrossRef]
52. Doan, T.C.; Majety, S.; Grenadier, S.; Li, J.; Lin, J.; Jiang, H. Fabrication and Characterization of Solid-State Thermal Neutron Detectors Based on Hexagonal Boron Nitride Epilayers. *Nucl. Instrum. Methods Phys. Res. A* **2014**, *748*, 84–90. [CrossRef]
53. Stoto, T.; Housseau, N.; Zuppiroli, L.; Kryger, B. Swelling and Microcracking of Boron-Carbide Subjected to Fast-Neutron Irradiations. *J. Appl. Phys.* **1990**, *68*, 3198–3206. [CrossRef]
54. Sun, J.; Zhu, H.; Wang, W.; Duan, Y. Effect of Boron Segregation on the Surface Crack of Low Carbon Boron-Bearing Steel. *Results Phys.* **2019**, *13*, 102153. [CrossRef]
55. Pan, J.; Wang, C.; Wang, Z.; Zhang, C.; Fang, L.; Li, J.; Mei, Q.; Gao, J.; Wang, M.; Li, H.; et al. Microstructure Characteristics and Properties of a Novel Ni-Based Alloy for Thermal Neutron and Gamma Ray Co-Shielding. *Mater. Charact.* **2024**, *210*, 113840. [CrossRef]
56. Chen, Z.; Huo, Z.; Zhang, H.; Zhong, G. Gamma Ray Shielding Composite Material with High Z Number. *Prog. Chem.* **2024**, *36*, 1102–1116.

Disclaimer/Publisher's Note: The statements, opinions and data contained in all publications are solely those of the individual author(s) and contributor(s) and not of MDPI and/or the editor(s). MDPI and/or the editor(s) disclaim responsibility for any injury to people or property resulting from any ideas, methods, instructions or products referred to in the content.